Field control of anisotropic spin transport and spin helix dynamics in a modulation-doped GaAs quantum well

S. Anghel,[1] F. Passmann,[1] A. Singh,[2] C. Ruppert,[1] A. V. Poshakinskiy,[3] S. A. Tarasenko,[3] J. N. Moore,[4] G. Yusa,[4] T. Mano,[5] T. Noda,[5] X. Li,[6] A. D. Bristow,[1,7] and M. Betz[1,*]

[1]*Experimentelle Physik 2, Technische Universität Dortmund, Otto-Hahn-Straße 4a, D-44227 Dortmund, Germany*
[2]*Department of Material Science and Engineering, Massachusetts Institute of Technology, Cambridge, Massachusetts 02139, USA*
[3]*Ioffe Institute, St. Petersburg 194021, Russia*
[4]*Department of Physics, Tohoku University, Sendai 980–8578, Japan*
[5]*National Institute for Materials Science, Tsukuba, Ibaraki 305-0047, Japan*
[6]*Texas Materials Institute, University of Texas at Austin, Austin, Texas 78712, USA*
[7]*Department of Physics and Astronomy, West Virginia University, Morgantown, West Virginia 26506-6315, USA*

Electron spin transport and dynamics are investigated in a single, high-mobility, modulation-doped, GaAs quantum well using ultrafast two-color Kerr-rotation microspectroscopy, supported by qualitative kinetic theory simulations of spin diffusion and transport. Evolution of the spins is governed by the Dresselhaus bulk and Rashba structural inversion asymmetries, which manifest as an effective magnetic field that can be extracted directly from the experimental coherent spin precession. A spin-precession length λ_{SOI} is defined as one complete precession in the effective magnetic field. It is observed that application of (i) an out-of-plane electric field changes the spin decay time and λ_{SOI} through the Rashba component of the spin-orbit coupling, (ii) an in-plane magnetic field allows for extraction of the Dresselhaus and Rashba parameters, and (iii) an in-plane electric field markedly modifies both the λ_{SOI} and diffusion coefficient.

I. INTRODUCTION

The relativistic phenomenon that is spin-orbit interaction (SOI) plays a central role in the behavior of spin transport and dynamics in semiconductors [1–3]. In noncentrosymmetric crystals, the conduction band is spin split by Dresselhaus SOI, originating from the bulk inversion asymmetry (BIA) [4]. Dresselhaus SOI in quantum wells (QWs) encompasses contributions that are linear and cubic in the carrier momentum $\mathbf{k}$. Additionally, carriers in heterostructures experience Rashba SOI, which arises from the structural inversion asymmetry (SIA) of the grown layer sequence [5] and is linear in momentum $\mathbf{k}$. These SOI components can be tailored in a QW by choosing an appropriate confinement potential. The Rashba SOI can also be externally tuned by applying a back-gate voltage, which affects the shape of the confinement potential.

SOI leads to a $\mathbf{k}$-dependent effective magnetic field $\mathbf{B}_{SOI}$ that electrons experience if they propagate through the crystal, resulting in Larmor precession of the electron spins around the effective magnetic field [6,7]. $\mathbf{B}_{SOI}$ can be expressed in terms of a spin-orbit coupling parameter, which we call the spin-precession length λ_{SOI}, corresponding to the distance over which the spin of a propagating electron completes one full rotation around the effective magnetic field.

SIA and BIA in [001]-oriented QWs can interfere and result in strong anisotropy of the spin splitting, particularly when the Rashba and Dresselhaus terms are of similar strength

[8,9]. Under these circumstances, the Dyakonov-Perel spin relaxation mechanism is suppressed for certain spin wave modes and a persistent spin helix (PSH) is formed, as predicted [10,11] and observed in GaAs QWs [12–15]. GaAs QWs can have a long spin decay time and high electron mobilities within the regime of strong SOI making it a good choice for study of SOIs.

λ_{SOI} incorporates both Rashba (α) and Dresselhaus (β) parameters. Typically, the Rashba contribution is more susceptible to changes of the band structure by external fields and/or photoexcitation. Information about the temporal [16] and back-gate voltage U_{BG} dependences [13,17] of λ_{SOI} has been obtained in recent scientific efforts addressing the PSH in QWs. In a recent study, some of the authors demonstrated that the lifetime of electron spins markedly depends on U_{BG}, i.e., on electron concentration [18]. However, the applied in-plane electric and magnetic field dependence of λ_{SOI} is still incomplete, with few examples of field control of the SOI [19]. For example it is unclear how λ_{SOI} depends on diffusion versus drift currents.

In this paper, we employ a time-resolved polar magneto-optic Kerr rotation microscopy technique to perform a comprehensive investigation of the dependence of λ_{SOI} on the in-plane electric and magnetic fields in a modulation-doped GaAs QW with high electron mobility exceeding 10^6 cm^2/V s, which is an order of magnitude larger than other recent work [19]. In a regime with BIA and SIA terms slightly detuned from the PSH conditions, we directly measure the diffusive evolution of a locally excited spin ensemble into a spin helix (SH) with shorter lifetime than the PSH.

*markus.betz@tu-dortmund.de

From experimental results, the dependence of λ_{SOI} on delay time, carrier density, back-gate voltage and the in-plane crystallographic direction are determined. It is found that λ_{SOI} substantially decreases over time while gradually approaching the SH precession length λ_0, which results from the finite laser spot size of pump and probe [20]. We also measure the dependence of λ_{SOI} on the back-gate voltage, which simultaneously tunes the electron concentration and the out-of-plane electric field along the growth direction, revealing a mostly linear dependence. In addition, we measure the dependence of λ_{SOI} on the carrier drift velocity v_{dr} by applying an in-plane electric field, finding a pronounced influence for in-plane fields even as small as $\sim 1\,\text{V/cm}$. In contrast, an applied in-plane magnetic field has minimal influence on the spin-diffusion coefficient or SOI.

We support these experimental finds with a kinetic theory of spin diffusion and PSH formation, which qualitatively reproduces the majority of the features observed in the experiments. Details of the theory are presented in the Appendix.

II. EXPERIMENT

The QW is grown by molecular beam epitaxy (MBE) on a highly n-doped [001] GaAs substrate. The width of the GaAs QW is $L_z = 15\,\text{nm}$, sandwiched between two $Al_{0.33}Ga_{0.67}As$ barriers. A growth interruption for Si-δ doping provides an electron concentration of $n \sim 1.9 \times 10^{11}\,\text{cm}^{-2}$ to form a two-dimensional electron gas (2DEG) with the estimated Fermi energy $\varepsilon_F \sim 7\,\text{meV}$ in the QW, relative to the bottom of the conduction band. The 2DEG density is increased by increasing U_{BG}.

The MBE-grown heterostructures is processed into a Hall-bar geometry with AuGeNi Ohmic contacts. The sample is cooled to $\sim 3.5\,\text{K}$ in a helium flow cryostat (Oxford Microstat HiRes2) where the spatial fluctuations are limited to a range that is negligible in comparison to the beam size.

For the analysis of spin dynamics in the QW, we use a magneto-optical Kerr rotation (KR) setup in a confocal reflection geometry. KR is a direct measure of the dynamic magnetization in the sample and, therefore, an ideal tool to study spin phenomena in 2DEGs [21]. Briefly, the output of a mode-locked femtosecond Ti-sapphire laser of 60 MHz repetition rate is split into pump and probe pulse trains. For independent wavelength tunability, each pulse trains through its own grating-based 4f-pulse-shaper [22].

The temporal resolution of the system is 1 ps, limited by the chosen spectral width (0.7 nm). For all results presented below, the pump beam is tuned to $\sim 1.57\,\text{eV}$ (790 nm) with a peak power density of $4.6\,\text{MW/cm}^2$ per pulse to effectively initialize a spin polarization while the probe is set to $\sim 1.53\,\text{eV}$ (807 nm) with a peak power density of $2.3\,\text{MW/cm}^2$ per pulse. The polarization state of the pump pulse is modulated between σ^+ and σ^- helicities using an electro-optical modulator (Qioptiq LM 0202P).

Both beams are collinearly focused onto the sample using a $50 \times$ objective (Mitutoyo M-Plan APO NIR), which offers a focused spot size for probe (pump) beams of $\sim 1(3)\,\text{mm}$. The reflected beams pass through a spectrometer, where the pump light is filtered out spectrally. The KR signal is measured in a standard balanced detection scheme. The amplitude of
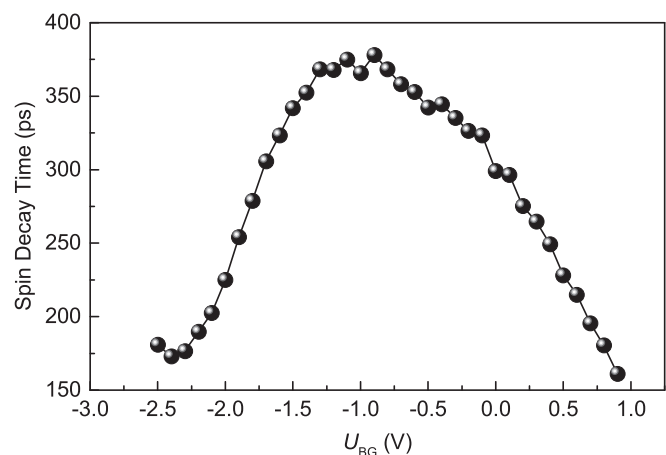

FIG. 1. Tunability of the spin decay time in the quantum well with back-gate voltage U_{BG}.

the signal is proportional to the rotation of the linear probe polarization caused by the magnetization associated with the pump induced spin polarization. Measurements on spin dynamics are undertaken as a function of delay time t between pump and probe pulses.

In order to record the spatial spin distribution $S_z(x, y)$, a telescope scheme is implemented in the pump arm. In particular, lateral motion of one of the lenses in the pump telescope allows scanning the excitation in the x and y directions relative to the probe [23,24]. Here, the x and y directions correspond to the $[1\bar{1}0]$ and $[110]$ crystallographic directions, respectively. An electromagnet supplies a magnetic field in the Voigt geometry. For drift dependent measurements, an additional in-plane electric field is applied using the Hall-bar contacts.

III. RESULTS AND DISCUSSION

A. Electron-density-dependent spin decay time

Figure 1 shows the electron spin decay time dependence on the back-gate voltage U_{BG}. The back-gate voltage varies the electron density n within the 2DEG, in an estimated range of $(10^{10} - 10^{11})\,\text{cm}^{-2}$. In addition to which, the optical excitation also induces photocarriers of similar concentrations determined using the equation $n = \frac{I_0 \cdot \tau}{E_{ph}} \cdot \frac{A}{\pi r^2}$ where $r = 1.5\,\mu\text{m}$ for the pump, $I_0 = 3.22\,\text{MW/cm}^2$ including a 30% Fresnel loss, $\tau = 1\,\text{ps}$, and $E_{ph} = 1.57\,\text{eV}$ and a QW absorbance ofxbrk A $\sim (1.5 - 6.0)\%$ [25].

The spin decay time is maximized for an intermediate carrier density, around $-1.4\,\text{V} < U_{BG} < -1.0\,\text{V}$, a result that is comparable to recent observations in similar structures [18,26]. Hence, subsequent measurements will be performed with $U_{BG} = -1.4\,\text{V}$, unless otherwise stated.

The nonmonotonic dependence of the spin decay time on U_{BG} stems primarily from modification of the Dyakonov-Perel spin relaxation mechanism, which is strongly suppressed in the range close to $-1.4\,\text{V}$ as the PSH is most efficiently formed. Away from this region, at strong negative voltages n is significantly decreased allowing excitons to form [18],
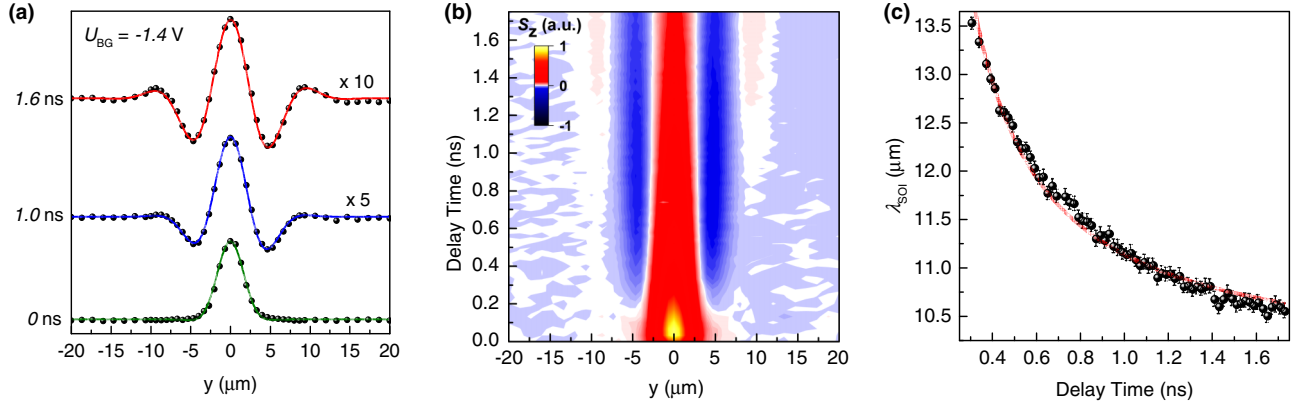
FIG. 2. (a) Normalized spatial spin-polarization distribution S_z measured along the y axis for various delay times and a constant back-gate voltage of $U_{BG} = -1.4$ V. The three data sets are normalized and vertically shifted for clarity. The solid lines represent fits according to Eq. (1). (b) Spatiotemporal evolution of $S_z(y,t)$ presented as false-color plot. (c) Temporal evolution of λ_{SOI} extracted with Eq. (1) from (b) and a solid fit line using Eq. (3).

and at close to zero voltages the increased n may also lead to additional carrier-carrier scattering [27].

B. Formation and evolution of the spin helix

The formation of a SH is conveniently visualized by tracking the spin polarization S_z in space and time. This effect is extracted by keeping the probe spot fixed and scanning the pump spot along the y direction for different delay times. Line scans $S_z(y,t)$ for three different values of t are shown in the Fig. 2(a). The first line $S_z(y, 0 \text{ ns})$ is recorded at the temporal overlap of the pump and probe pulses. The spatial profile of the spin polarization corresponds to a convolution of pump and probe spot and is approximately Gaussian. The photoexcited electron spin ensemble expands in time due to carrier diffusion.

In Fig. 2(a), $S_z(y, 1 \text{ ns})$ and $S_z(y, 1.6 \text{ ns})$ feature a stripe pattern consisting of an alternating sign of $S_z(y,t)$, which is caused by the spin precession around the effective magnetic field $\boldsymbol{B}_{SOI}$. A more detailed set of the $S_z(y)$ scans for a range of delay times is shown as a false-color plot in Fig. 2(b). It is evident that the excited spin polarization $\boldsymbol{S}$ starts with $\boldsymbol{S}||z$ and then oscillates as a function of y as the electrons diffuse away from $y = 0$. A full oscillation of S_z starts to emerge for delay times $t > 1.5$ ns. To quantify the combined effect of expanding Gaussian profiles and the SH oscillations, the experimental data $S_z(y,t)$ are fitted to the product of a Gaussian and a cosine [16,18]

$$S_z(y) = A \cdot e^{-\frac{4\ln(2)(y-y_0)^2}{w^2}} \cdot \cos\left(\frac{2\pi(y - y_1)}{\lambda_{SOI}}\right), \quad (1)$$

where w and y_0 are the full width at half maximum (FWHM) and center positions of the Gaussian peak and y_1 is the spatial phase of the oscillatory function.

The width of the Gaussian envelope is expected to increase with delay time due to carrier diffusion, according to [27]

$$w^2(t) = w_0^2 + 16\ln(2)D_s t, \quad (2)$$

where D_s is the spin-diffusion coefficient, w_0 is the initial FWHM determined by the laser spot sizes on the sample. A linear fit of the beam waist $w^2(t)$ (data not shown) provides a direct measure of D_s. We obtain a value of $D_s =$

$57.3 \text{ cm}^2\text{ s}^{-1}$ ($w_0 = 3.3\,\mu\text{m}$) comparable to previous reports on similar QWs [28].

Figure 2(c) displays the transient $\lambda_{SOI}(t)$, which reveals a decrease from 13.5 µm initially, towards $\sim 10.5\,\mu\text{m}$ after a delay time of >1 ns. This decrease is well described by the time dependence [20]

$$\lambda_{SOI}(t) = \lambda_0 \left(1 + \frac{w_0^2}{16 \cdot \ln(2) \cdot D_s \cdot t}\right) \quad (3)$$

after ~ 0.28 ns when the evolution of S_z allows for resolution of λ_{SOI} in Eq (1). The fit (red line) yields a precession length of the SH mode of $\lambda_0 = 9.9\,\mu\text{m}$ and a spin-diffusion coefficient of $D_s = 74 \text{ cm}^2\text{ s}^{-1}$; the latter is slightly larger compared to the value obtained from the $w^2(t)$ dependence. This difference is attributed to the sample being slightly detuned from the PSH regime (see Sec. III C), which becomes evident from separate fittings of Eq. (2) and Eq. (3). Prior to addressing more detailed questions we will discuss the physics behind this spatial spin precession.

The oscillation is dependent on the SIA and BIA contributions to SOI, arising from the geometry and material of the experiment. The lack of space inversion symmetry in zinc-blende-type structures, such as GaAs QWs, lifts the spin degeneracy of the conduction band. This phenomenon is quantified by a spin- and momentum-dependent contribution to the Hamiltonian that can be interpreted as an effective magnetic field $\boldsymbol{B}_{SOI}$ acting on propagating electron spins [7]. Choosing the Cartesian axes in the QW plane to be $x \parallel [1\bar{1}0]$ and $y \parallel [110]$, $\boldsymbol{B}_{SOI}$ can be written as

$$\boldsymbol{B}_{SOI} = \frac{2}{g\mu_B}\begin{pmatrix}[\alpha + \beta] \cdot k_y \\ [\beta - \alpha] \cdot k_x\end{pmatrix}, \quad (4)$$

where k_x and k_y are the in-plane wave vectors, g is the effective g factor, μ_B is the Bohr magneton, and α (β) is the Rashba (Dresselhaus) parameter related to the strength of the SIA (BIA).

In the envelope function approach, $\beta = -\gamma_D[\langle k_z^2 \rangle - k_F^2/4]$. where γ_D is the Dresselhaus coupling constant, $\langle k_z^2 \rangle = (\pi/L_z)^2 = 0.04 \text{ nm}^{-2}$ is a lower bound for the first term and $k_F = \sqrt{2\pi n}$, such that $k_F^2/4 \sim 0.003 \text{ nm}^{-2}$ when estimated
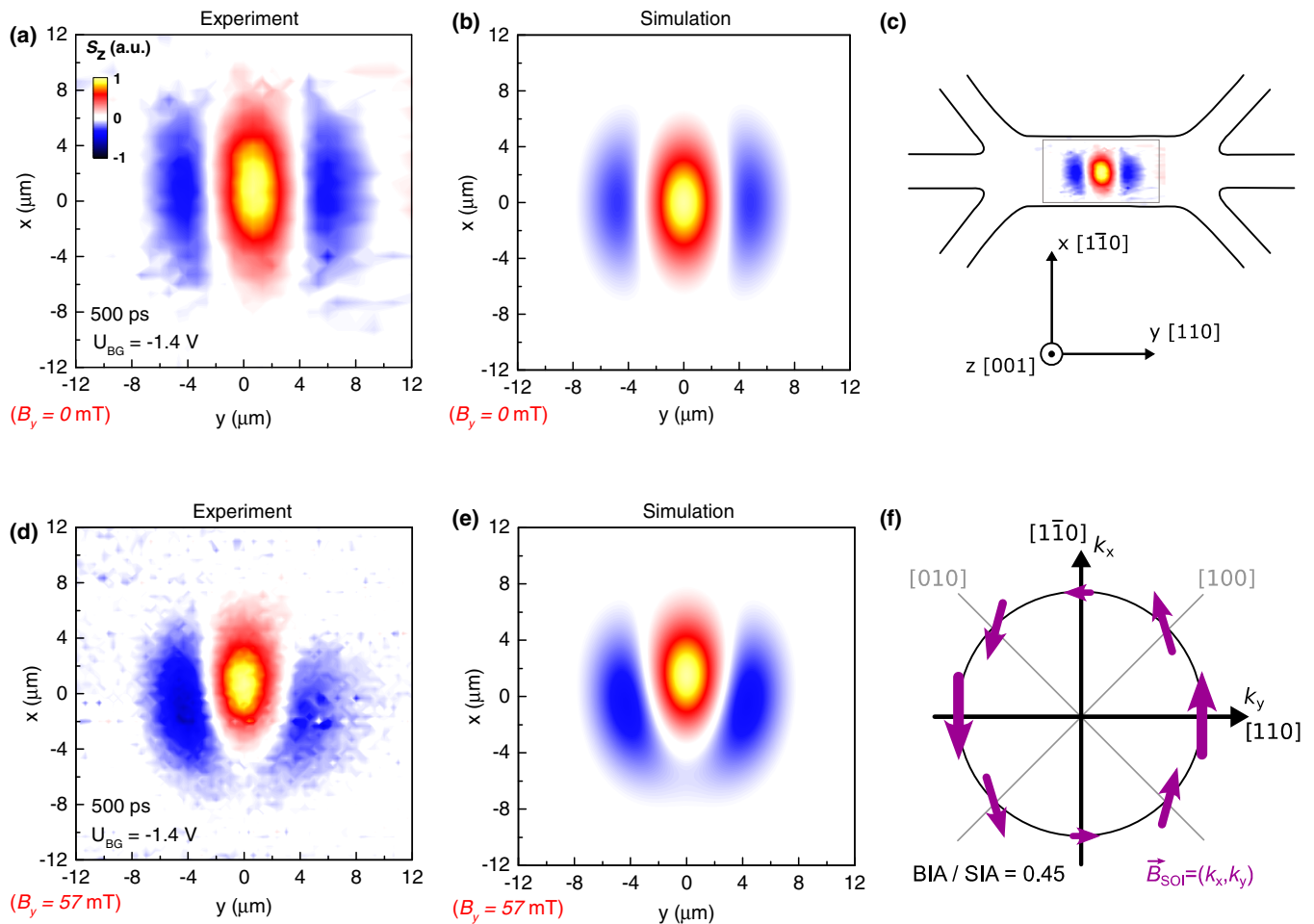
FIG. 3. Experimentally measured and simulated two-dimensional spatial maps of the spin polarization S_z due to diffusive transport. Data is obtained for the back-gate voltage of $U_{BG} = -1.4$ V and at a delay time of 0.5 ns without external magnetic field (a) and (b) and $B_y = 57$ mT (d) and (e) respectively. The pattern in the absence of the field results from the formation of a spin helix along the y axis, while an applied external magnetic field allows precession to take place also along the x axis. The simulated maps are obtained by numerically solving Eq. (A6) for the set of parameters extracted from measurements. (c) Schematic visualization of the map in (a) on the sample surface (inserted false-color plot magnified for improved visualization). (f) Orientation and magnitude of the effective magnetic field B_{SOI} in k space on the Fermi surface, plotted for the ratio of $a/b = 0.45$ with zero applied magnetic field, matching (a) and (b).

with the zero-bias electron density. The Rashba parameter $\alpha = \gamma_R E_z$ is related to the internal electric field E_z oriented in the growth direction of the QW, which can be tuned by the U_{BG}. Meanwhile, the tuning induces also changes in the 2DEG density and screening effects, which could in turn affect the E_z.

B_{SOI} can be examined through two-dimensional spatial maps of the spin polarization $S_z(x, y)$; see the false-color representation in Fig. 3(a) and its orientation with respective to the Hall bar in Fig. 3(c). The figures show the spatial spread of S_z due to diffusion in the plane of the QW for $t = 500$ ps. The spatial map exhibits an oscillating pattern arising from the spin precession of diffusing carriers around B_{SOI}. The stripelike pattern in Fig. 3(a) clearly shows that only electrons propagating along [110], i.e., y direction, undergo a significant spin precession. The underlying anisotropy of B_{SOI} in k space is visualized in Fig. 3(f). This directional dependence of B_{SOI} is calculated for a ratio of the SIA and BIA contributions of $\alpha/\beta = 0.45$. This configuration results in a strong effective

magnetic field experienced by electrons traveling along the y axis, whereas electrons traveling along the x axis experience almost no B_{SOI}.

When $\alpha/\beta \rightarrow 1$, at the Fermi level, the anisotropy becomes even stronger as B_{SOI} vanishes for the electrons propagating along the x direction. In this balanced regime, $\alpha = \beta$ gives rise to the SU(2) spin rotation symmetry within the 2DEG, supporting a PSH and extending the spin decay time. From the absence of an oscillatory spin pattern along the x axis, it is confirmed that the Rashba and Dresselhaus parameters are of the same order of magnitude for $U_{BG} = -1.4$ V.

Parameters of the long-lived spin mode can be calculated in the framework of the kinetic theory described in the Appendix. For the diffusive transport regime and $\alpha \cdot \beta > 0$, the spin-precession length is given by

$$\lambda_0^{-1} = \frac{m^*}{\pi \hbar^2} |\alpha + \beta| \sqrt{1 - \frac{1}{16} \tan^4\left(\phi - \frac{\pi}{4}\right)}, \quad (5)$$
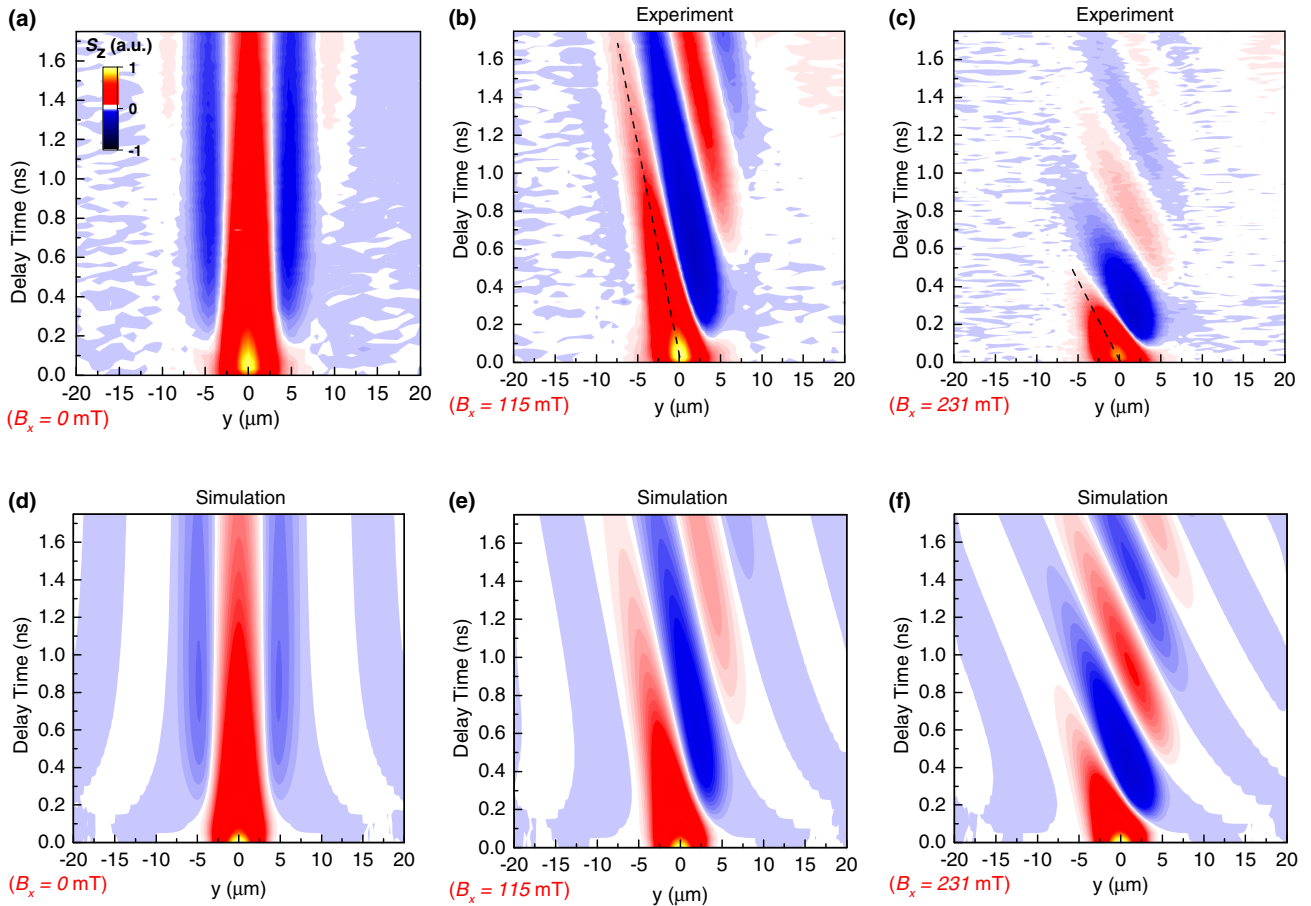
FIG. 4. Experimental spatiotemporal maps of the evolution of $S_z(y,t)$ for $U_{BG} = -1.4$ V and B_x (oriented along the [1$\bar{1}$0] direction) equal to (a) 0 mT, (b) 115 mT, and (c) 231 mT. The dashed lines indicate the time dependence of the center position y_0, which is the position of constant phase within the spin precession. Theoretical simulations, based on Eq. (A6), are displayed in (d), (e), and (f) for magnetic field strengths corresponding to those in the experiments.

where m^* is the electrons effective mass, $\hbar$ is Plank's constant divided by 2π and the phase is $\phi = \arctan(\alpha/\beta)$. Hence, spatial mapping of the spin precession allows for a quantitative determination of $\boldsymbol{B}_{SOI}$ by the sum $|\alpha + \beta|$.

C. Applied in-plane magnetic-field dependence

The individual α, β parameters can be extracted from the anisotropy of the two-dimensional spatial maps in the presence of an external magnetic field. Comparison of the maps with and without the external magnetic field, applied in the y direction, shows an additional oscillation in the x direction with the field. From the best fit of the experimental data at $B_y = 0$ [Fig. 3(a)] and $B_y = 57$ mT [Fig. 3(d)], employing the drift-diffusion equation [Eq. (A6) of the Appendix], we extract $\alpha = 1.1 \times 10^{-11}$ eV cm, $\beta = 2.5 \times 10^{-11}$ eV cm and $D_s = 64$ cm^2/s.

Figures 3(b) and 3(e) show simulations of spatial distributions of S_z calculated from the extracted experimental parameters, with an effective g factor $= 0.03$ and a Gaussian excitation spot with a FWHM of 3.3 μm. These simulations reproduce all the essential features of the experimental $S_z(x,y)$, demonstrating the power of the kinetic approach. It should be noted that the false-color plots for both experiment and theory have the same scale.

In the presence of an external magnetic field $\boldsymbol{B} \parallel x$, we obtain information about the spin precession in the (yz) plane. The resulting temporal evolution of $S_z(y)$ is shown in Fig. 4 for B_x equal to 0 mT [Fig. 4(a)], 115 mT [Fig. 4(b)], and 231 mT [Fig. 4(c)]. Application of B_x tilts the stripe pattern observed without the field, indicating a temporal shift of a given peak position (corresponding to a fixed orientation of the spins) towards $y < 0$. Fitting the data to Eq. (1) reveals a linear dependence of the parameter y_1 on t, due to a constant velocity of the carriers in the applied field. The tilted time-evolution arises from the motion of electrons and the cancellation of $B_{SOI}(k_y)$ by B_x. Consequently, for an electron with the exact momentum $\hbar k_y = m^* \, dy_1/dt$, precession is suppressed as it propagates.

Taking into consideration Eq. (4) and the condition $B_x = B_{SOI}$, velocity in the y direction is

$$\frac{dy_1}{dt} = \frac{\hbar g \mu_B}{2m^*(\alpha + \beta)} \cdot B_x, \tag{6}$$

As a result, the analysis of Fig. 4 gives direct access to $[\alpha + \beta]$. Specifically, we analyze the temporal derivative of the fit parameter y_1 for different values of B_x. Figure 5(a) shows the expected linear trend. From the slope of the linear dependence (dashed line) we find a strength of the SOI coupling of $\alpha + \beta =$
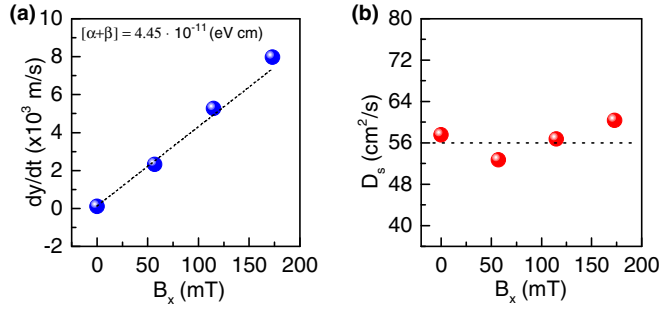
FIG. 5. (a) Effective velocity of the phase offset y_1 for several magnetic field strengths B_x. The dashed line is a linear fit. (b) Spin-diffusion coefficient for different values of B_x. The dashed line is a guide to the eye.

4.45×10^{-11} eV cm. This value is in good agreement with the one ($\alpha + \beta = 3.85 \times 10^{-11}$ eV cm) obtained from Eq. (5), by using $\lambda_0 = 9.9\,\mu$m [value previously obtained, see Eq. (3)]. In addition, by comparing the decay of the signals in Fig. 4(a) with those in Fig. 4(b) and 4(c), it can be seen that the spin coherence suffers from field-induced dephasing. Furthermore, the spin-diffusion coefficient is not markedly influenced by moderate values of B_x, see Fig. 5(b). Finally, the temporal

evolution of the SH density distribution $S_z(y,t)$ is reproduced by the kinetic theory simulations [Figs. 4(d)–4(f)] for the same magnetic fields used in the experiment and using the same fit parameters as used in Fig. 3.

D. Applied in-plane electric-field dependence

The Hall-bar structure permits a weak electric field E_y to be applied in the plane of the QW. E_y drives a drift current that is expected to increase the distance over which coherent spin dynamics can be measured. Figure 6(a) depicts spatiotemporal data for an in-plane electric field of –0.9 V/cm. Initially, the electron motion is driven by diffusion and drift currents, the latter of which drags the electrons towards the positive y direction. There is also a slight tilt in the stripes that is a consequence of oscillation in time of the spin polarization (for fixed y), referred to as ω [19] and which is proportional to $y_1/\lambda_{\mathrm{SOI}}$. The value of ω is E_y dependent and proportional to the β_3 Dresselhaus term. Moreover, the tilt increases as a function of time as the periodicity of the S_z increases, which is in accordance with variation in $\lambda_{\mathrm{SOI}}(t)$ presented in Fig 2(c). Visual inspection of Figs. 6(a) and 4(a) clearly indicates that λ_{SOI} is smaller with an applied field for the same delay time. Quantitative comparison of Fig. 6(c) and Fig. 2(c) confirms this.

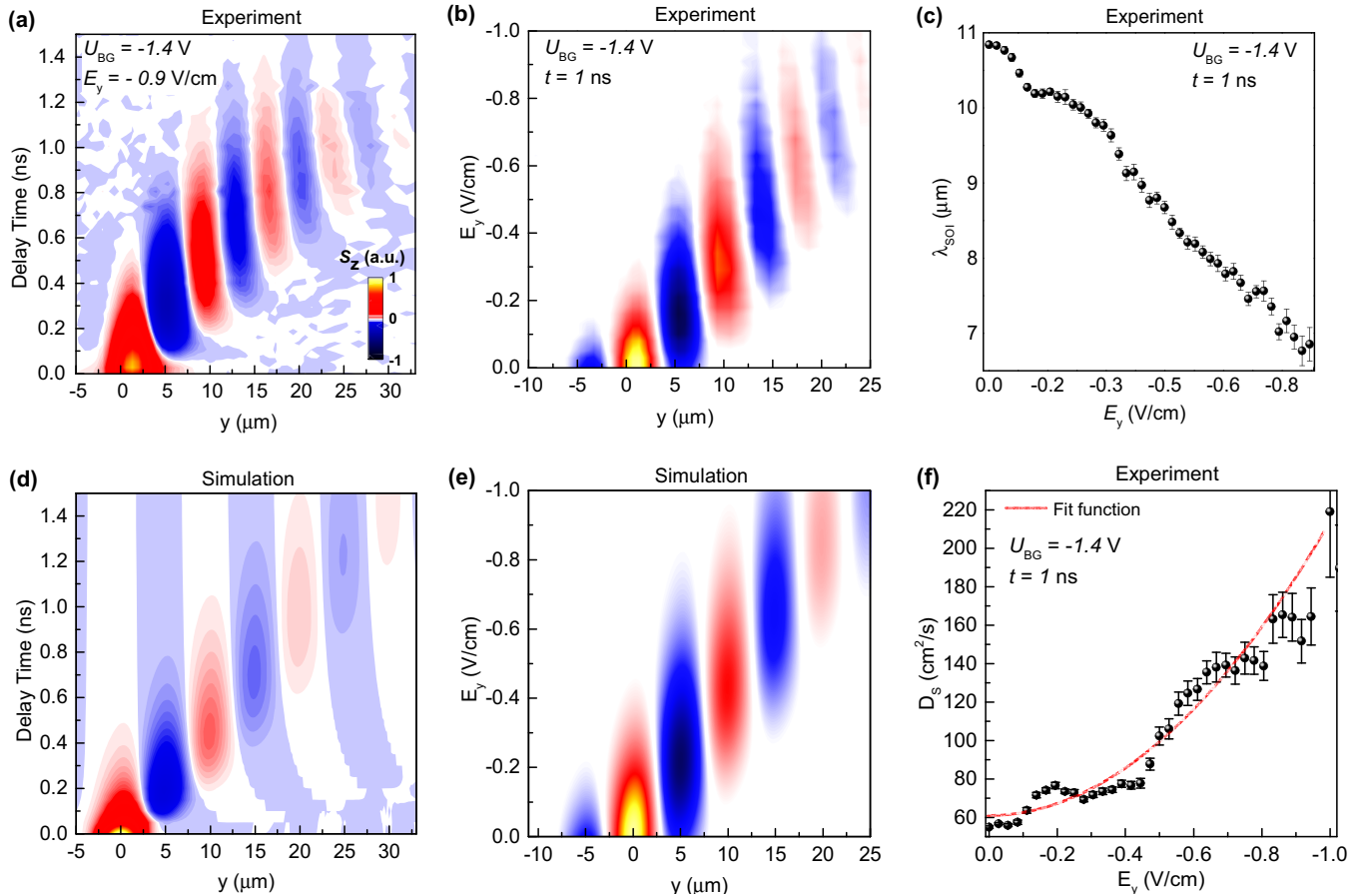
FIG. 6. In-plane electric field dependence of the electron spin evolution: (a) Experimental and (d) simulated false-color plots of $S_z(y,t)$ for $E_y = -0.9$ V/cm. (b) Experimental and (e) simulated plots of $S_z(y,E_y)$ for $t = 1$ ns. Experimental results recorded with $U_{\mathrm{BG}} = -1.4$ V and simulations determined from Eq. (A6). (c) Electric field dependence of λ_{SOI} extracted by fitting the data of (b) using Eq. (1). (f) Dependence of the spin-diffusion coefficient D_s on E_y, fit by a second-order polynomial function (red curve).

Figure 6(d) shows a simulation of the spatiotemporal map with an in-plane electric field. For simplicity, this simulation uses previously determined Rashba and Dresselhaus parameters at $E_y = 0$ V/cm and $D_s = 170$ cm^2/s extracted at $E_y = -0.9$ V/cm. The simulation reproduces the overall $+y$ displacement of the electron ensemble due to drift, the stripes and tilt of the moving spin pattern.

Variation in $\lambda_{SOI}(t)$ with and without the applied in-plane electric field warrants direct study of $\lambda_{SOI}(E_y)$. Hence, Fig. 6(b) shows the dependence of $S_z(y, E_y)$ for $t = 1$ ns, when the motion is dominated only by the drift current. Electrons move towards positive y values with increasing E_y and produce a tilt of the striped pattern, due to an additional decrease in λ_{SOI} with increasing E_y. The increased periodicity of $S_z(y, E_y)$ allows for a better fit for w, λ_{SOI}, y_0, and y_1, even at small t. $\lambda_{SOI}(E_y)$ is extracted from the experiment by fitting $S_z(y, E_y)$ with Eq. (1) and plotted in Fig. 6(c). The data support a decreasing trend of λ_{SOI} with increasing applied field magnitude $|E_y|$ (data for $E_y > 0$ not shown).

We identify three main mechanisms that may lead to an E_y-dependent λ_{SOI}: (i) experimentally determined variations in D_s with E_y adjusts λ_{SOI} in accordance with Eq. (3); (ii) E_y alters a due to inadvertent components to E_z; and (iii) contributions to b that depend on drift velocity (see the Supplemental Material of Ref. [19]) become significant for high mobilities. The following discussion addresses each of these mechanisms in the context of our results.

(i) Electron motion may increase spin dephasing due to an increased scattering rate. In fact, it is evident in Fig. 6(b) that the amplitude of $S_z(y)$ decreases with increasing drift velocity, suggesting an increased spin dephasing. Within the Dyakonov-Perel mechanism, the decrease in spin decay time for fixed SOI parameters, suggests an increase of the spin-diffusion coefficient D_s [29]. Such an increase of D_s resulting from the in-plane electric field is indeed observed in the experiment; see Fig. 6(f). The in-plane electric field dependence of D_s is fit by a second-order polynomial function, matching the increase of D_s by a factor of three at $E_y = -1$V/cm. According to Eq. (3) the threefold change of D_s would only lead to a 3% decrease of λ_{SOI}, which is insufficient to explain the results seen in Fig. 6(c).

For comparison, D_s remains approximately two orders of magnitude lower than the charge diffusion coefficient $D_e \sim 10^4$ cm^2/s, indicating the role of electron-electron scattering [30,31]. D_e is estimated from the mobility $\mu \sim 1.5 \times 10^6$ cm^2/(Vs) and the Fermi energy $\varepsilon_F = 7$ meV.

(ii) The sample geometry could impart a component of the in-plane electric field into the growth direction, which potentially alters λ_{SOI} through the Rashba component that depends on E_z. To verify the likelihood of this idea, we examine the dependence of λ_{SOI} on the back-gate voltage. Figure 7(a) shows $S_z(y, U_{BG})$ at $t = 500$ ps and $E_y = -1$ V/cm. In this measurement, E_y is applied to ensure electron transport and access $m(U_{BG})$.

In the range -2.9 V $< U_{BG} < -1.9$ V, y_0 remains close to $y = 0$, which is attributed to localization of the remaining electron in the QW that do not return to the doping layer in the presence of strong E_z. This is seen spectroscopically as a recovery of neutral exciton features in photoluminescence [18]. For $U_{BG} < -1.9$ V, y_0 becomes positive as the electron

concentration increases and delocalization occurs. The change in y_0 is exhibited as the striped pattern in $S_z(y, U_{BG})$. This picture is corroborated by the dependence of $m(U_{BG})$; see Fig. 7(b). Mobility is determined using $\mu = v_{dr}/E_y$, where the drift velocity $v_{dr} = y_0/t$ is experimentally extracted from $S_z(y)$ by tracking y_0 with Eq (1). It is observed that μ is small for $U_{BG} < -1.9$ V as a result of localization, above this voltage m grows $> 50\times$ as delocalization occurs.

Figure 7(c) shows the dependence of λ_{SOI} on U_{BG}, determined by fitting $S_z(y, U_{BG})$ with Eq. (1). The magnitude of λ_{SOI} decreases almost linearly as U_{BG} is tuned from 0 V to -2 V. This behavior can be attributed to the Rashba contribution of λ_{SOI}, which is linearly dependent on the applied E_z, as described in relation to Eq. (4). Simultaneously, U_{BG} changes the electron density n, which might result in an additional contribution to a due to Coulomb screening. Consequently, the nonlinear behavior of $\lambda_{SOI}(U_{BG})$ may result from the interplay of these inseparable contributions.

Regardless of the existence of any component of E_y on U_{BG}, the observed change of λ_{SOI} on U_{BG} is rather small compared to its direct dependence on E_y. For a change in $E_y = 0.8$ V/cm, which corresponds to an in-plane bias of 1.3 V, there is a 4.5 mm change in $\lambda_{SOI}(E_y)$. By contrast $\lambda_{SOI}(U_{BG})$ shows only a 3 mm change for a 3 V change in U_{BG}. Hence, variation of the spin-precession length due to the in-plane electric field is a more significant effect than that caused by U_{BG}. Also, as it was pointed above, λ_{SOI} decreases with increasing the applied in-plane electric field magnitude $|E_y|$, which would not be the case for a monotonic change in α due to E_y. This confirms that E_y indeed directly modifies the spin-precession length.

(iii) $\boldsymbol{B}_{SOI}$ can include terms that depend on the electronic drift and diffusion currents via the Dresselhaus SOI [19]. Consequently, $\boldsymbol{B}_{SOI}$ and hence l_{SOI} can be modified by sufficiently large drift velocity. $v_{dr} = \mu E_y \sim 20$ km/s at $|E_y| = 1$ V/cm, which is only one order of magnitude smaller than the Fermi velocity $v_F = \hbar k_F/m^* = 297$ km/s, determined from $\beta_3 = \hbar^2\omega/(2m^* v_{dr}) = 8.2 \times 10^{-12}$ eV cm giving $n = 4.7 \times 10^{11}$ cm^{-2}, and an order of magnitude larger than the initial diffusion velocity $v_{Di} \sim 4$ km/s, determined from differentiation of the evolution of the half-width half maximum $w(t)/2$ of Fig 2(b).

As pointed out in the Supplementary Material of Ref. [19], higher-order harmonic contributions to ω are small, estimated to be on the order of 4% due to the ratio $(k_{dr}/k_F)^2$. While these contributions are neglected, it is possible that they play a role when the drift velocity is sufficiently high or the electron sheet density is small. However, the drift-velocity-dependent contributions to $\boldsymbol{B}_{SOI}$ are insufficiently large to account for the observed $l_{SOI}(E_y)$.

IV. CONCLUSIONS

In summary, we have studied the anisotropic spin transport and spin helix formation in a modulation-doped GaAs-based quantum well. Spatiotemporal analysis of the spin polarization as a function of back-gate voltage and in-plane electric field reveals a tunability of the spin-precession length λ_{SOI} with both in-plane and out-of-plane electric fields. The decay of λ_{SOI} with delay time is correlated with the survival of the long-lived spin helix mode.
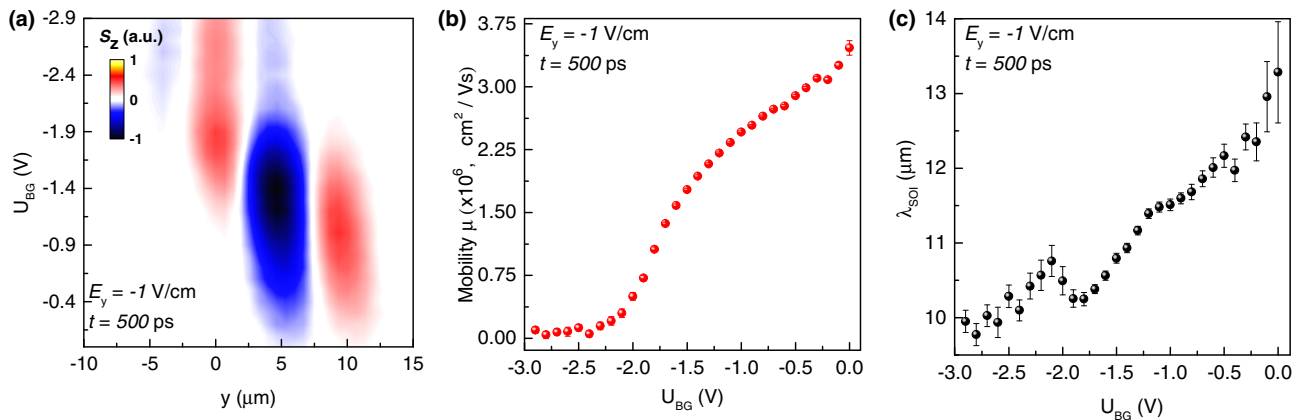
FIG. 7. (a) Spatial evolution of $S_z(y, U_{BG})$ for in-plane electrical field $E_y = -1.0$ V/cm and delay time of 500 ps. Extracted values of back-gate voltage-dependent (b) electron mobility μ and (c) spin-precession length λ_{SOI}.

Tuning the back-gate voltage induces changes to out-of-plane electric field that results in a mostly linear dependence of λ_{SOI}. In addition, a pronounced decrease of λ_{SOI} occurs when applying an in-plane electric field. This latter result warrants further study because the change of λ_{SOI} cannot be attributed to direct or indirect modification of the spin-orbit coupling by an altered diffusion coefficient. The observed threefold increase in the spin-diffusion coefficient with the applied in-plane electric field, is also insufficient to modify the observed change in λ_{SOI}. In contrast, application of a moderate external magnetic field does not significantly influence the spin-orbit interactions or the spin-diffusion coefficient.

Note added. Recently, the authors became aware of an in-plane electric-field dependence of the spin dynamics; see Kunihashi *et al.*, Phys. Rev. Lett. **119**, 187703 (2017). This work confirms that there are indeed regimes where the PSH can be manipulated with in-plane electric fields and the resulting drift velocity.

APPENDIX

The experimentally observed spin-diffusion and spin helix formation can be described in the framework of the kinetic equation for the spin distribution function in the wave vector and real spaces $s(\boldsymbol{k}, \boldsymbol{r}, t)$ that has the form

$$\frac{\partial \boldsymbol{s}}{\partial t} + \frac{e}{\hbar}\left(\boldsymbol{E} \cdot \frac{\partial}{\partial \boldsymbol{k}}\right)\boldsymbol{s} + \left(\boldsymbol{v}_k \cdot \frac{\partial}{\partial \boldsymbol{r}}\right)\boldsymbol{s}$$
$$= (\boldsymbol{\Omega}_k + \boldsymbol{\Omega}_L) \times \boldsymbol{s} + \text{St}[\boldsymbol{s}], \quad \text{(A1)}$$

where e is the electron charge, $\boldsymbol{v}_k = \hbar \boldsymbol{k}/m^*$ is the electron velocity, $\boldsymbol{\Omega}_k(\boldsymbol{\Omega}_L)$ is the spin-precession frequency around the effective magnetic field (external magnetic field), and $\text{St}[\boldsymbol{s}_k]$ is the collision integral. The collision integral describes the scattering of electrons by QW imperfections as well as electron-electron scattering. In the collision-dominated regime, when $\boldsymbol{\Omega}_k \tau \ll 1$, where τ is the scattering time, the spin distribution function is given by the sum of $\boldsymbol{k}$-isotropic and $\boldsymbol{k}$-anisotropic terms, $\boldsymbol{s}(\boldsymbol{k}, \boldsymbol{r}, t) = \bar{\boldsymbol{s}}(\varepsilon_k, \boldsymbol{r}, t) + \delta \boldsymbol{s}(\boldsymbol{k}, \boldsymbol{r}, t)$ with $\delta \boldsymbol{s} \ll \bar{\boldsymbol{s}}$. Here, the bar denotes averaging over the directions of the wave vector $\boldsymbol{k}$ and $\varepsilon_k = \hbar^2 k^2/(2m^*)$ is the electron energy. We assume the energy relaxation is faster than the spin relaxation so that the electron system is thermalized and the $\boldsymbol{k}$-isotropic part of the spin-distribution function has the form

$$\bar{\boldsymbol{s}}(\varepsilon, \boldsymbol{r}, t) \propto \boldsymbol{S}(\boldsymbol{r}, t)\frac{d}{d\varepsilon}f_{\text{FD}}(\varepsilon), \quad \text{(A2)}$$

where $\boldsymbol{S}(\boldsymbol{r}) = \sum_k \bar{\boldsymbol{s}}(\varepsilon_k, \boldsymbol{r})$ is the local spin density and $f_{\text{FD}}(\varepsilon)$ is the Fermi-Dirac function. Summing up Eq. (A1) over $\boldsymbol{k}$ and neglecting spin relaxation due to the scattering we obtain the equation for the spin density

$$\frac{\partial \boldsymbol{S}}{\partial t} = \boldsymbol{\Omega}_L \times \boldsymbol{S} + \sum_k \left[\boldsymbol{\Omega}_k \times \delta \boldsymbol{s} - \left(\boldsymbol{v}_k \cdot \frac{\partial}{\partial \boldsymbol{r}}\right)\delta \boldsymbol{s}\right]. \quad \text{(A3)}$$

The anisotropic part of the spin-distribution function is found from the equation

$$\text{St}[\delta \boldsymbol{s}] = \left(\boldsymbol{v}_k \cdot \frac{\partial}{\partial \boldsymbol{r}}\right)\bar{\boldsymbol{s}} + \frac{e}{\hbar}\left(\boldsymbol{E} \cdot \frac{\partial}{\partial \boldsymbol{k}}\right)\bar{\boldsymbol{s}} - \boldsymbol{\Omega}_k \times \bar{\boldsymbol{s}}, \quad \text{(A4)}$$

which, in the τ approximation, yields

$$\delta \boldsymbol{s} = \tau_p^* \boldsymbol{\Omega}_k \times \bar{\boldsymbol{s}} - \tau_p^*\left(\boldsymbol{v}_k \cdot \frac{\partial}{\partial \boldsymbol{r}}\right)\bar{\boldsymbol{s}} - \tau_p e(\boldsymbol{E} \cdot \boldsymbol{v}_k)\frac{\partial \bar{\boldsymbol{s}}}{\partial \varepsilon}. \quad \text{(A5)}$$

Here, τ_p is the momentum relaxation time, which determines the electron mobility and is governed by electron

scattering from QW imperfections, and τ_p^* is the scattering time, which determines spin diffusion and is limited by both electron scattering from QW imperfections and electron-electron scattering [30]. Combining Eqs. (A3) and (A5) we obtain the drift-diffusion equation for the spin density

$$\frac{\partial \boldsymbol{S}}{\partial t} + \left(\boldsymbol{v}_{\mathrm{dr}} \cdot \frac{\partial}{\partial \boldsymbol{r}} \right) \boldsymbol{S} = D_s \frac{\partial^2 \boldsymbol{S}}{\partial \boldsymbol{r}^2} - \boldsymbol{\Gamma} \boldsymbol{S} - \left(\boldsymbol{\Lambda} \frac{\partial}{\partial \boldsymbol{r}} \right)$$
$$\times \boldsymbol{S} + (\boldsymbol{\Omega}_L + \boldsymbol{\Omega}_{\mathrm{dr}}) \times \boldsymbol{S}. \quad \text{(A6)}$$

Here, $\boldsymbol{v}_{\mathrm{dr}} = \langle \partial (\varepsilon \tau_p) / \partial \varepsilon \rangle e \boldsymbol{E} / m^*$ is the drift velocity, $D_s = \langle v^2 \tau_p^* \rangle / 2$ is the spin-diffusion coefficient,

$$\Gamma_{\alpha\beta} = \left\langle \left(\boldsymbol{\Omega}_{\boldsymbol{k}}^2 \delta_{\alpha\beta} - \Omega_{\boldsymbol{k},\alpha} \Omega_{\boldsymbol{k},\beta} \right) \tau_p^* \right\rangle \quad \text{(A7)}$$

is the Dyakonov-Perel spin-relaxation-rate tensor;

$$\Lambda_{\alpha\beta} = 2 \langle \overline{\Omega_{\boldsymbol{k},\alpha} v_{\boldsymbol{k},\beta}} \tau_p^* \rangle \quad \text{(A8)}$$

is the tensor describing the spin precession during diffusion;

$$\boldsymbol{\Omega}_{\mathrm{dr}} = \left\langle \frac{d}{d\varepsilon} \tau_p \overline{(e\boldsymbol{E} \cdot \boldsymbol{v}_k) \boldsymbol{\Omega}_k} \right\rangle \quad \text{(A9)}$$

is the spin-precession frequency during drift, and the angle brackets denote the energy averaging,

$$\langle A \rangle = \frac{\int A \frac{d f_{\mathrm{FD}}}{d\varepsilon} d\varepsilon}{\int \frac{d f_{\mathrm{FD}}}{d\varepsilon} d\varepsilon}. \quad \text{(A10)}$$

By solving Eq. (A6) with the given spin-orbit coupling parameters one can calculate the temporal evolution and spatial distribution of the electron spin density, also in the presence of external electric and magnetic fields. The results of such numerical solutions for the parameters extracted from experimental data are plotted in Figs. 3, 4, and 6 and demonstrate good agreement with the experiments.

For [001]-oriented QWs, the effective spin-orbit field lies in the QW plane and is given by Eq. (4). The presence of both Rashba and Dresselhaus SOI terms leads to an anisotropy of the spin splitting and the spin helix formation. At long enough delay times, the spatial distribution of spin density is determined by spin density waves with the longest lifetime. In particular, in the absence of external electric and magnetic fields, the longest lifetime (for $\alpha \cdot \beta > 0$) is achieved for the spin density wave along y with the wave vector

$$q_0 = \frac{2m^*}{\hbar^2} |\alpha + \beta| \sqrt{1 - \frac{1}{16} \tan^4 \left(\phi - \frac{\pi}{4} \right)}, \quad \text{(A11)}$$

where $\phi = \arctan |\alpha/\beta|$ [3]. The corresponding length of spin precession is given by $\lambda_0 = 2\pi/q_0$.

The in-plane magnetic field modifies the spin density distribution. In a strong enough magnetic field, the longest lifetime is achieved for the mode with the wave vector $\boldsymbol{q}$, for which the direction of the effective spin-orbit magnetic field coincides with the direction of the external magnetic field $\boldsymbol{\Lambda} \boldsymbol{q} \parallel \boldsymbol{\Omega}_L$. For the external magnetic field pointing along the x axis, the long-lived spin density wave propagates along the y axis and has the wave vector

$$q_0(\boldsymbol{\Omega}_L \parallel x) = \frac{2m^*}{\hbar} |\alpha + \beta| \quad \text{(A12)}$$

while for the magnetic field oriented along the y axis the wave propagates along the x axis and has the wave vector

$$q_0(\boldsymbol{\Omega}_L \parallel y) = \frac{2m^*}{\hbar} |\alpha - \beta|. \quad \text{(A13)}$$

Thus, from the periods of spatial spin oscillations at zero magnetic field and magnetic field pointed along y axis we can determine both Rashba and Dresselhaus constants independently.

---

[1] V. V. Bel'kov *et al.*, Phys. Rev. Lett. **100**, 176806 (2008).

[2] M. Kohda *et al.*, Phys. Rev. B **86**, 081306(R) (2012).

[3] A. V. Poshakinskiy and S. A. Tarasenko, Phys. Rev. B **92**, 045308 (2015).

[4] G. Dresselhaus, Phys. Rev. **100**, 580 (1955).

[5] E. I. Rashba, Fiz. Tverd. Tela (Leningrad) **2**, 1224 (1960).

[6] A. Manchon, H. C. Koo, J. Nitta, S. M. Frolov, and R. A. Duine, Nature Mater **14**, 871 (2015).

[7] M. I. Dyakonov and Yu. V. Kachorovskii, Fiz. Techn. Poluprov. **20**, 178 (1986).

[8] B. Jusserand, D. Richards, G. Allan, C. Priester, and B. Etienne, Phys. Rev. B **51**, 4707 (1995).

[9] S. D. Ganichev and L. E. Golub, Phys. Status Solidi B **251**, 1801 (2014).

[10] B. A. Bernevig, J. Orenstein, and S. C. Zhang, Phys. Rev. Lett. **97**, 236601 (2006).

[11] V. N. Gridnev, J. Exp. Theor. Phys. Lett. **76**, 502 (2002).

[12] A. Sasaki, S. Nonaka, Y. Kunihashi, M. Kohda, T. Bauernfeind, T. Dollinger, K. Richter, and J. Nitta, Nature Nanotechnol. **9**, 703 (2014).

[13] J. Ishihara, Y. Ohno, and H. Ohno, Appl. Phys. Express **7**, 013001 (2014).

[14] J. D. Koralek, C. P. Weber, J. Orenstein, B. A. Bernevig, S.-C. Zhang, S. Mack, and D. D. Awschalom, Nature (London) **458**, 610 (2009).

[15] M. Kohda and G. Salis, Semicond. Sci. Technol. **32**, 073002 (2017).

[16] M. P. Walser, C. Reichl, W. Wegscheider, and G. Salis, Nature Phys. **8**, 757 (2012).

[17] G. Wang, B. L. Liu, A. Balocchi, P. Renucci, C. R. Zhu, T. Amand, C. Fontaine, and X. Marie, Nature Commun. **4**, 2372 (2013).

[18] S. Anghel, A. Singh, F. Passmann, H. Iwata, J. N. Moore, G. Yusa, X. Q. Li, and M. Betz, Phys. Rev. B **94**, 035303 (2016).

[19] P. Altmann, F. G. Hernandez, G. J. Ferreira, M. Kohda, C. Reichl, W. Wegscheider, and G. Salis, Phys. Rev. Lett. **116**, 196802 (2016).

[20] G. Salis, M. P. Walser, P. Altmann, C. Reichl, and W. Wegscheider, Phys. Rev. B **89**, 045304 (2014).

[21] S. A. Crooker, D. D. Awschalom, J. J. Baumberg, F. Flack, and N. Samarth, Phys. Rev. B **56**, 7574 (1997).

[22] A. Singh, G. Moody, S. Wu, Y. Wu, N. J. Ghimire, J. Yan, D. G. Mandrus, X. Xu, and X. Li, Phys. Rev. Lett. **112**, 216804 (2014).

[23] T. Henn, T. Kiessling, W. Ossau, L. W. Molenkamp, K. Biermann, and P. V. Santos, Rev. Sci. Instrum. **84**, 123903 (2013).

[24] T. Henn, T. Kießling, L. W. Molenkamp, D. Reuter, A. D. Wieck, K. Biermann, P. V. Santos, and W. Ossau, Phys. Status Solidi B **251**, 1839 (2014).

[25] J. Hegarty, L. Goldner, and M. D. Sturge, Phys. Rev. B **30**, 7346 (1984).

[26] I. Y. Gerlovin *et al.*, Phys. Rev. B **75**, 115330 (2007).

[27] L. M. Smith, D. R. Wake, J. P. Wolfe, D. Levi, M. V. Klein, J. Klem, T. Henderson, and H. Morkoç, Phys. Rev. B **38**, 5788 (1988).

[28] H. Zhao, M. Mower, and G. Vignale, Phys. Rev. B **79**, 115321 (2009).

[29] M. I. Dyakonov, *Spin physics in semiconductors* (Springer, Berlin, 2008).

[30] I. D'Amico and G. Vignale, Phys. Rev. B **62**, 4853 (2000).

[31] R. Völkl, M. Griesbeck, S. A. Tarasenko, D. Schuh, W. Wegscheider, C. Schüller, and T. Korn, Phys. Rev. B **83**, 241306(R) (2011).